

# Examination of the $^{22}\text{C}$ radius determination with interaction cross sections

T. Nagahisa<sup>1</sup> and W. Horiuchi<sup>1</sup>

<sup>1</sup>*Department of Physics, Hokkaido University, Sapporo 060-0810, Japan*

A nuclear radius of  $^{22}\text{C}$  is investigated with the total reaction cross sections at medium- to high-incident energies in order to resolve the radius puzzle in which two recent interaction cross section measurements using  $^1\text{H}$  and  $^{12}\text{C}$  targets show the quite different radii. The cross sections of  $^{22}\text{C}$  are calculated consistently for these target nuclei within a reliable microscopic framework, the Glauber theory. To describe appropriately such a reaction involving a spatially extended nucleus, the multiple scattering processes within the Glauber theory are fully taken into account, that is, the multi-dimensional integration in the Glauber amplitude is evaluated using a Monte Carlo technique without recourse to the optical-limit approximation. We discuss the sensitivity of the spatially extended halo tail to the total reaction cross sections. The root-mean-square matter radius obtained in this study is consistent with that extracted from the recent cross section measurement on  $^{12}\text{C}$  target. We show that the simultaneous reproduction of the two recent measured cross sections is not feasible within this framework.

## I. INTRODUCTION

Advances in the radioactive ion beam facility have revealed the exotic structure of short-lived neutron-rich unstable nuclei, which has never been observed in stable nuclei, such as halo structure [1]. The neutron dripline of carbon isotopes is observed to be at  $^{22}\text{C}$ , which is known to be the heaviest two-neutron halo nucleus has been found so far. This nucleus is a key to the understanding of the shell evolution along the neutron dripline with the magicity at the neutron number 14 ( $^{20}\text{C}$ ) and 16 ( $^{22}\text{C}$ ). The three-body  $^{20}\text{C} + n + n$  system is the so-called Borromean, in which neither of the subsystems,  $^{20}\text{C}-n$  and  $n-n$ , are bound, leading to an extended two-neutron wave function with  $s$ -wave dominance predicted by the earlier three-body calculation [2]. In fact, the two-neutron separation energy observed is very small:  $0.42 \pm 0.94$  MeV [3] and  $0.14 \pm 0.46$  MeV [4]. The  $s$ -wave two-neutron halo structure is further confirmed by the  $^{20}\text{C}$  fragment momentum distribution measurement of the two neutron removal reaction from  $^{22}\text{C}$  [5]. This nucleus has attracted much attention not only to nuclear physics but also atomic physics in connection to the Efimov physics [6, 7].

A research interest has now been extended to reveal the exotic excitation mechanism of  $^{22}\text{C}$  [8–10]. However, the experimental situation on the  $^{22}\text{C}$  radius, which is one of the most important and basic properties of an atomic nucleus, has been still under discussion. Since direct electron-scattering measurement is not feasible at the moment, and a neutron radius is difficult to probe, the nuclear radii of unstable nuclei have often been studied by the total reaction or interaction cross sections at medium- and high-incident energies (several tens MeV to 1 GeV). The first measurement of the interaction cross section of  $^{22}\text{C}$  was performed in 2010 by Tanaka *et al.* [11]. The large interaction cross section on  $^1\text{H}$  target incident at 40 MeV/nucleon was measured  $1338 \pm 274$  mb, resulting in a huge matter radius of  $5.4 \pm 0.9$  fm with large uncertainties. Recently, high-precision measurement was made for the interaction cross section on  $^{12}\text{C}$  target incident at

$\sim 240$  MeV/nucleon by Togano *et al.* [12], and the resultant radius is  $3.44 \pm 0.08$  fm, which is quite far from the previously extracted value  $5.4 \pm 0.9$  fm [11]. Since the nuclear radius has often served as one of the inputs to some theoretical models, e.g., Refs. [6, 7, 13], this demands appropriate reliable evaluation of the nuclear radius.

Here we focus on the theoretical investigation of the nuclear radius of  $^{22}\text{C}$  with the total reaction cross sections. Use of such inclusive observables has some advantages: The theory of describing the cross section is well established; and the cross sections can be measured for almost all nuclei as long as the beam intensity is sufficient; and the different sensitivity to the nuclear density profile can be controlled by a choice of a target nucleus and an incident energy. Systematic analyses of nuclear matter radii with the total reaction cross sections on  $^{12}\text{C}$  target incident at  $\gtrsim 200$  MeV/nucleon have revealed structure changes and the role of excess neutrons of light neutron-rich unstable nuclei [14–21]. We remark that the total reaction cross sections on  $^1\text{H}$  target is also useful because the probe has different sensitivity to protons and neutrons in the projectile nucleus depending on incident energies that can be used to extract the neutron-skin thickness of unstable nuclei [22, 23].

In this paper, we evaluate the nuclear radius of a two neutron halo nucleus,  $^{22}\text{C}$ , from the total reaction cross sections on  $^1\text{H}$  and  $^{12}\text{C}$  targets, and discuss the sensitivity of the halo tail to these cross sections. We employ a reliable high-energy reaction theory, the Glauber model [24], which is a microscopic multiple-scattering theory starting from the total nucleon-nucleon cross section. In this work, the complete evaluation of the Glauber amplitude is made by using a Monte Carlo technique in order to treat the extended two-neutron halo wave function of  $^{22}\text{C}$  appropriately. Also, we test the optical-limit-approximation (OLA), a standard approximation of the Glauber model, which has been used in many analyses of the radius extraction (See Appendix for references), and quantify the possible uncertainties with this approximation.

The paper is organized as follows. Sec. II briefly ex-

plains the Glauber model employed in this paper. The Glauber amplitude which involves multi-dimensional integration is introduced in this section. Sec. III is devoted to the evaluation of the multi-dimensional integration using the Monte Carlo technique. The explicit expression of the Glauber amplitude is presented in Sec. III A. Sec. III B explains how to generate the wave function of  $^{22}\text{C}$ . Monte Carlo configurations that crucially determine the accuracy of the multi-dimensional integration are generated in Sec. III C. They are tested in the total reaction cross section calculations in Sec. III D. Our results are presented and discussed in Sec. IV. A direct comparison between the theoretical and experimental cross sections is made. In Sec. IV A, the validity of our calculations is confirmed with available experimental data of  $^{12}\text{C}+^{12}\text{C}$  and  $^{12}\text{C}+^1\text{H}$  systems. Then, we further confirm the reliability of our calculations in the reactions involving  $^{20}\text{C}$  and  $^{12}\text{C}$ . Sec. IV B presents our main results: We describe the  $^{22}\text{C}+^{12}\text{C}$  and  $^{22}\text{C}+^1\text{H}$  reactions in a consistent manner and discuss the possible uncertainties in the radius extraction using the total reaction cross section. The sensitivity of the halo tail of  $^{22}\text{C}$  to the total reaction cross sections is also discussed. The conclusion is drawn in Sec. V. A detailed analysis of approximate treatment of the Glauber amplitude is given in Appendix.

## II. TOTAL REACTION CROSS SECTION IN THE GLAUBER MODEL

Here we consider a high-energy collision of the projectile ( $P$ ) and target ( $T$ ) nuclei with mass numbers  $A_P$  and  $A_T$ , respectively. The Glauber model [24] is a microscopic multiple-scattering theory which is widely used to study high-energy nucleus-nucleus collisions. With the help of the adiabatic and eikonal approximations, the final state wave function of a projectile and target system,  $\Phi_f$ , is greatly simplified as the product of the ground-state wave functions of the projectile  $\Phi_0^P$  and the target  $\Phi_0^T$  nuclei, and the multiple-product of the phase-shift functions of a nucleon-nucleon collision,  $e^{i\chi_{NN}}$ , as

$$|\Phi_f\rangle = \exp \left[ i \sum_{j=1}^{A_P} \sum_{k=1}^{A_T} \chi_{NN}(\mathbf{b} + \hat{\mathbf{s}}_j^P - \hat{\mathbf{s}}_k^T) \right] |\Phi_0^P \Phi_0^T\rangle, \quad (1)$$

where  $\mathbf{b}$  is the impact parameter vector perpendicular to the beam direction  $z$ , and  $\hat{\mathbf{s}}_j^P$  ( $\hat{\mathbf{s}}_k^T$ ) denotes the two-dimensional single-particle coordinate operator projected onto the  $xy$ -plane of the  $j$ th ( $k$ th) nucleon from the center-of-mass, abbreviated as cm, of the projectile (target).

With this approximation, we only need to evaluate the optical phase-shift function or the Glauber amplitude,  $e^{i\chi(\mathbf{b})}$ , which includes all information of the elastic pro-

cesses in the high-energy nuclear collision

$$e^{i\chi(\mathbf{b})} = \langle \Phi_0^P \Phi_0^T | \prod_{j=1}^{A_P} \prod_{k=1}^{A_T} [1 - \Gamma_{NN}(\mathbf{b} + \hat{\mathbf{s}}_j^P - \hat{\mathbf{s}}_k^T)] | \Phi_0^P \Phi_0^T \rangle, \quad (2)$$

where the profile function  $\Gamma_{NN}(\mathbf{b}) = 1 - e^{i\chi_{NN}(\mathbf{b})}$  is introduced for the sake of convenience. The total reaction cross section is evaluated by integrating the reaction probability

$$P(\mathbf{b}) = 1 - |e^{i\chi(\mathbf{b})}|^2, \quad (3)$$

over  $\mathbf{b}$  as

$$\sigma_R = \int d\mathbf{b} P(\mathbf{b}). \quad (4)$$

The profile function is usually parametrized as [25]

$$\Gamma_{NN}(\mathbf{b}) = \frac{1 - i\alpha_{NN}}{4\pi\beta_{NN}} \sigma_{NN}^{\text{tot}} \exp \left[ -\frac{\mathbf{b}^2}{2\beta_{NN}} \right], \quad (5)$$

where  $\sigma_{NN}^{\text{tot}}$ ,  $\alpha_{NN}$ , and  $\beta_{NN}$  are the total nucleon-nucleon ( $NN$ ) cross section, the ratio between the real and imaginary parts of the scattering amplitude at the forward angle, and the so-called slope parameter, respectively. Parameter sets for various incident energies are listed in Ref. [26] for proton-proton ( $pp$ ) and proton-neutron ( $pn$ ) are employed. The  $nn$  ( $np$ ) are taken to be the same as  $pp$  ( $pn$ ). For the sake of simplicity, hereafter we omit  $NN$  in the profile function otherwise needed. The validity of the parameter sets of the profile function has already been confirmed in a number of examples [18, 22, 23, 27–29]. The other inputs to the theory are the wave functions of projectile and target nuclei. Once these inputs are set, the theory has no adjustable parameter. We do not consider the Coulomb breakup contributions since the effects are negligible in systems involving small  $Z$  nuclei [23, 27].

## III. EVALUATION OF MULTI-DIMENSIONAL INTEGRATION IN THE GLAUBER AMPLITUDE

In general, the explicit evaluation of the Glauber amplitude of Eq. (2) is difficult because the expression involves  $3(A_P + A_T)$ -dimensional integration. For  $^1\text{H}$  target, it is possible to reduce the dimension of the integral in the Glauber amplitude when the projectile wave function is represented by some specific forms such as a Gaussian form [30] or a Slater determinant of single-particle wave functions [28, 31–33]. For nucleus-nucleus scattering, the explicit evaluation is in general tedious, and thus one has to introduce some approximations to reduce the complexity. However, it is known that the standard optical-limit approximation cannot be applied to nucleus-nucleus reactions involving spatially extended nuclei, leading to systematic uncertainties on the extraction of the nuclear radii [34, 35] (See also Appendix of this

paper). On the contrary, a Monte Carlo (MC) integration offers a direct way to evaluate the multi-dimensional integration in the Glauber amplitude of Eq. (2) [36–38]. We take the same route as the MC integration succeeds in its complete evaluation.

### A. Multi-dimensional integration in the Glauber amplitude

The multi-dimensional integration in Eq. (2) is evaluated using the MC integration. For this purpose, we introduce the  $A$ -body density

$$\rho_A(\bar{\mathbf{r}}_1, \dots, \bar{\mathbf{r}}_A) = \langle \Phi_0 | \prod_{i=1}^A \delta(\hat{\mathbf{r}}_i - \bar{\mathbf{r}}_i) | \Phi_0 \rangle, \quad (6)$$

where  $\hat{\mathbf{r}}_i$  is the single-particle coordinate operator of the  $i$ th nucleon from the origin. Then, the complete Glauber amplitude of Eq. (2) reads

$$\begin{aligned} e^{i\chi(\mathbf{b})} &= \int \dots \int \left( \prod_{j=1}^{A_P} d\bar{\mathbf{r}}_j^P \right) \left( \prod_{k=1}^{A_T} d\bar{\mathbf{r}}_k^T \right) \\ &\times \rho_{A_P}^P(\bar{\mathbf{r}}_1^P, \dots, \bar{\mathbf{r}}_{A_P}^P) \rho_{A_T}^T(\bar{\mathbf{r}}_1^T, \dots, \bar{\mathbf{r}}_{A_T}^T) \\ &\times \prod_{j=1}^{A_P} \prod_{k=1}^{A_T} [1 - \Gamma(\mathbf{b} + \mathbf{s}_j^P - \mathbf{s}_k^T)], \end{aligned} \quad (7)$$

where  $\mathbf{s}_j^P$  ( $\mathbf{s}_k^T$ ) denotes the  $xy$ -component of the  $j$ th ( $k$ th) single-particle coordinate from the cm coordinate of the projectile (target). The product of the  $A$ -body densities of the projectile and target nuclei,  $\rho_{A_P}^P \rho_{A_T}^T$ , is the guiding function of the MC integration. If appropriate MC configurations are given, Eq. (7) can easily be evaluated by summing up  $\prod_{i=1}^{A_P} \prod_{j=1}^{A_T} [1 - \Gamma(\mathbf{b} + \mathbf{s}_i^P - \mathbf{s}_j^T)]$  with these MC configurations at each  $\mathbf{b}$ . Since the many-body operator,  $\prod_{i=1}^{A_P} \prod_{j=1}^{A_T} [1 - \Gamma(\mathbf{b} + \hat{\mathbf{s}}_i^P - \hat{\mathbf{s}}_j^T)]$ , is translationally invariant, i.e., free from the cm motion, the cm wave functions in  $\Phi_0^P$  and  $\Phi_0^T$  are integrated out through the MC integration. For spherical projectile and target nuclei, the integration over  $\mathbf{b}$  in Eq. (4) is reduced to one-dimensional one over  $|\mathbf{b}|$  which is performed simply by the trapezoidal rule.

### B. Wave function

The wave function is assumed to be the product of antisymmetrized neutron and proton wave functions

$$\Phi_0 = (\mathcal{A}_n \Phi_n) (\mathcal{A}_p \Phi_p) \quad (8)$$

with  $\mathcal{A}_N$  being the antisymmetrizer for proton ( $N = p$ ) and neutron ( $N = n$ ) defined by

$$\mathcal{A}_N = \frac{1}{\sqrt{\mathcal{N}_N!}} \sum_{(p_1, \dots, p_{\mathcal{N}_N})}^{\mathcal{N}_N!} \text{sgn}(p_1, \dots, p_{\mathcal{N}_N}) P_{(p_1, \dots, p_{\mathcal{N}_N})}, \quad (9)$$

where the operator  $P_{(p_1, \dots, p_{\mathcal{N}_N})}$  exchanges particle indices and  $\mathcal{N}_N$  denotes the number of proton or neutron. For the sake of simplicity, we assume for  $\Phi_N$  the product of the single-particle wave function  $\phi_i(\bar{\mathbf{r}}_i)$  of the  $i$ th nucleon

$$\Phi_N = \prod_{i=1}^{\mathcal{N}_N} \phi_i(\bar{\mathbf{r}}_i). \quad (10)$$

In the present work, we have considered the three nuclei,  $^{12}\text{C}$ ,  $^{20}\text{C}$ , and  $^{22}\text{C}$ . A configuration of the  $^{12}\text{C}$  wave function is assumed to be  $(0s_{1/2})^2(0p_{3/2})^4$  for both proton and neutron with the harmonic-oscillator (HO) single-particle wave functions. Since the charge radius of  $^{12}\text{C}$  is well known, the HO length parameter can be fixed in such a way so as to reproduce the point-proton radius, 2.33 fm extracted from the charge radius [39]. For  $^{20}\text{C}$  and  $^{22}\text{C}$ , single particle wave functions of  $^{20}\text{C}$  and  $^{22}\text{C}$  systems are generated from the phenomenological Woods-Saxon potential [40, 41]

$$V(r) = -V_0 f(r) + V_1 (\hat{\mathbf{l}} \cdot \hat{\mathbf{s}}) \frac{1}{r} \frac{d}{dr} f(r) + V_C(r), \quad (11)$$

where  $f(r) = 1 / \{1 + \exp[(r - R_N)/a]\}$  with  $a = 0.65 \text{ fm}$ ,  $R_N = 1.25 A^{1/3} \text{ fm}$ .  $V_0$  is taken commonly for proton and neutron, and  $V_1 = 0.6875 V_0$ .  $V_C$  is the Coulomb potential with a uniform charge distribution with a sphere radius  $R_N$ , which only acts on a proton.

We explain how we take the strength  $V_0$  in the following: A proton configuration is assumed to be  $(0s_{1/2})^2(0p_{3/2})^4$ . The subshell closure of the neutron number 14 and 16 is assumed for neutron configurations of  $^{20}\text{C}$  and  $^{22}\text{C}$  and are taken respectively as  $(0s_{1/2})^2(0p_{3/2})^4(0p_{1/2})^2(0d_{5/2})^6$  for  $^{20}\text{C}$  and  $(0s_{1/2})^2(0p_{3/2})^4(0p_{1/2})^2(0d_{5/2})^6(1s_{1/2})^2$  for  $^{22}\text{C}$ . These assumptions can be reasonable to describe  $^{22}\text{C}$  as  $^{20}\text{C} + n + n$   $s$ -wave two-neutron halo structure [2] which is confirmed by the  $^{20}\text{C}$  fragment momentum distribution measurement of the two neutron removal reaction from  $^{22}\text{C}$  [5]. To simulate the two neutron halo structure of  $^{22}\text{C}$ , we firstly take  $V_0$  commonly to all angular-momentum  $l$  states and fix it in such a way so as to reproduce the interaction reaction cross section of  $^{20}\text{C} + ^{12}\text{C}$  measured at  $\sim 900 \text{ MeV}$  [42]. Since a small  $V_0$  value for  $l = 0$  ( $V_0^{l=0}$ ) generates the single-particle wave function with a long tail that crucially determines the radius of the  $^{22}\text{C}$ , we only vary  $V_0^{l=0}$  as a free parameter that controls the radius of  $^{22}\text{C}$ .

To perform the MC integration accurately, we need to generate a large number of points, typically  $10^6$ – $10^8$ , which follow the probability distribution  $\rho_{A_P}^P \rho_{A_T}^T$  but indeed it costs computational resources because we have to take care of  $(\mathcal{N}_p^P! \mathcal{N}_n^P! \mathcal{N}_p^T! \mathcal{N}_n^T!)^2$  permutations for the projectile and target wave functions coming from the bra and ket sides. In order to reduce the computational cost, we consider to use the simple-product wave function defined by Eq. (10). Note that in the present case this assumption does not change any one-body physical quantities such as nuclear radius and one-body density but

the  $A$ -body density of Eq. (6) is modified resulting in some cross section differences through the Glauber amplitude of Eq. (7). We confirm that the difference in the total reaction cross sections on  $^1\text{H}$  target with the fully-antisymmetrized and the simple-product wave functions for  $^{20}\text{C}$  is small typically less than  $\sim 1\%$ . Therefore, for the practical reason, we employ the simple-product wave functions of  $^{20}\text{C}$  and  $^{22}\text{C}$  as Eq. (10).

### C. Monte Carlo configurations and nuclear radius

The guiding function of the MC integration, the  $A$ -body density (6), is constructed by a random walk with the Metropolis algorithm [43]. The number of spatial points (MC configurations) represented in Cartesian coordinate  $(x_1, y_1, z_1, \dots, x_A, y_A, z_A)$  are generated by the random walk with the step size  $\Delta$ . The resulting MC configurations must follow the probability distribution or the guiding function. They are used to perform the multi-dimensional integration over projectile and target coordinates. The accuracy of the MC integration crucially depends on the number of MC configurations  $M$  and a choice of  $\Delta$ . Since the total reaction cross section is closely related to the nuclear size, the MC configurations used in this paper are required to reproduce at least the root-mean-square matter radius (rms radius) of the  $^{22}\text{C}$  defined by

$$\sqrt{\langle \bar{r}^2 \rangle} = \sqrt{\frac{1}{A} \sum_{i=1}^A \int d\bar{r} |\bar{r}|^2 |\phi_i(\bar{r})|^2} \quad (12)$$

with  $A = 22$ . We remark that the above expression (12) involves the cm contribution. Though we exactly exclude the cm contribution through the MC integration later, this uncorrected radius can be used for a purpose to evaluate the precision of the MC integration. As the wave function assumed in this paper is defined by the product of the single-particle wave functions, the integration becomes simple which can also be evaluated accurately by a standard integration method, the trapezoidal rule.

To optimize  $\Delta$ , we generate several probability distributions for  $^{22}\text{C}$  with different  $\Delta$  values and calculate the rms radii defined in Eq. (12) by the MC integration. Then, they are compared with the “exact” rms radii evaluated with the direct integration in Eq. (12) by the trapezoidal rule. Finally, we set  $\Delta = 1.0 \text{ fm}$  that minimizes the rms deviations of the rms radii of  $^{22}\text{C}$  evaluated with the exact and the MC integration ranging from  $\sim 3$  to  $4 \text{ fm}$ . We note that in such extended wave functions the optimal  $\Delta$  value is larger than that for a typical wave function. In fact,  $\Delta = 0.25 \text{ fm}$  is used as the optimal value for  $^{12}\text{C}$  whose wave function is not much extended.

Figure 1 displays the cm uncorrected rms radii of  $^{22}\text{C}$  as a function of the potential strengths  $-V_0^{l=0}$  with different number of the MC configurations. The exact rms radii are also plotted for comparison. We confirm that desired MC configurations are successfully generated with

an appropriate choice of  $\Delta$ , that is, all the MC configurations with  $M = 10^6$ – $10^8$  reproduce perfectly the exact rms radii. We will make further tests of these MC configurations for the multi-dimensional integration in the Glauber amplitude in the next subsection. The cm corrected rms radii of  $^{22}\text{C}$  are also plotted in Fig. 1 with  $M = 10^8$ , which can be obtained by evaluating the multi-dimensional integration

$$\sqrt{\langle \bar{r}^2 \rangle} = \sqrt{\frac{1}{A} \sum_{i=1}^A \int \cdots \int \prod_{j=1}^A d\bar{r}_j |\bar{r}_i|^2 \rho_A(\bar{r}_1, \dots, \bar{r}_A)}. \quad (13)$$

Taking  $\rho_A(\bar{r}_1, \dots, \bar{r}_A)$  as the guiding function, one can easily perform the multi-dimensional integration by summing up  $|\bar{r}_i|^2$  ( $\bar{r}_i = \bar{r}_i - \mathbf{X}$  with  $\mathbf{X} = \frac{1}{A} \sum_{i=1}^A \bar{r}_i$ ) using a set of the MC configurations. The difference between the cm corrected and uncorrected radii appears to be large typically  $\sim 0.1 \text{ fm}$ , which cannot be neglected for the realistic calculations.

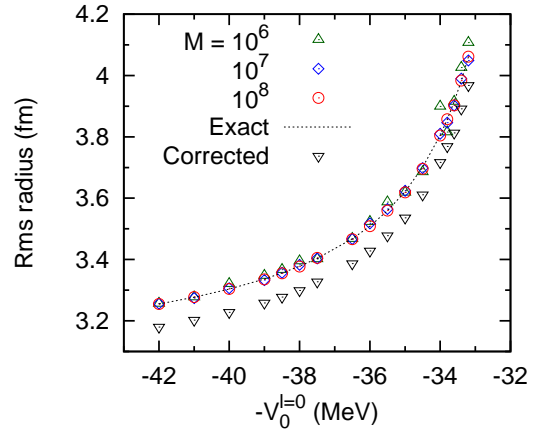


FIG. 1: Rms radii of  $^{22}\text{C}$  as a function of potential strengths for  $l = 0$  with different number of Monte Carlo configurations,  $M$ . Exact calculations with the center-of-mass (cm) contribution are plotted for comparison. The cm-free rms radii with  $M = 10^8$  (Corrected) are also plotted for comparison. See text for details.

### D. Tests of Monte Carlo configurations in the total reaction cross section calculations

Here we test the accuracy of the MC integration in the total reaction cross section calculations with respect to the number of the MC configurations. For  $^1\text{H}$  target, when the projectile wave function is represented by the product of the single-particle wave functions, we can factorize the expression and evaluate the complete Glauber amplitude without recourse to the MC integra-



tion as [28, 31]

$$e^{i\tilde{\chi}(\mathbf{b})} = \langle \Phi_0 | \prod_{j=1}^A [1 - \Gamma(\mathbf{b} + \hat{\mathbf{s}}_j)] | \Phi_0 \rangle \quad (14)$$

$$= \int \cdots \int \left( \prod_{j=1}^A d\tilde{\mathbf{r}}_j \right) \times \rho_A(\tilde{\mathbf{r}}_1, \dots, \tilde{\mathbf{r}}_A) \prod_{j=1}^A [1 - \Gamma(\mathbf{b} + \tilde{\mathbf{s}}_j)] \quad (15)$$

$$= \prod_{j=1}^A \left[ 1 - \int d\tilde{\mathbf{r}} \phi_j^*(\tilde{\mathbf{r}}) \Gamma(\mathbf{b} + \tilde{\mathbf{s}}) \phi_j(\tilde{\mathbf{r}}) \right]. \quad (16)$$

Eq. (15) is the explicit form for the MC integration, while in Eq. (16) one can simply use the trapezoidal rule for the integration over  $\tilde{\mathbf{r}}$ . Obviously, the above Glauber amplitude includes the cm contribution but the expression is useful for a test of the MC integration as was done in the previous subsection.

The incident energies are chosen as 40 MeV and 240 MeV for  $^1\text{H}$  and  $^{12}\text{C}$  targets, respectively, where the experimental data are available. Here the incident energy is measured in MeV per nucleon and for simplicity is written in MeV throughout this paper. Figure 2 compares the total reaction cross sections on  $^1\text{H}$  target evaluated with different numbers of the MC configurations as a function of the cm uncorrected rms radii. In order to make a direct comparison with the expression of Eqs. (15) and (16), they are respectively evaluated by the MC and trapezoidal (Exact) integration. Though all the wave functions give almost the same rms radius as shown in Fig. 1, the cross sections shows somewhat scattered distributions, depending on the number of the MC configurations, with  $M = 10^6$  and  $10^7$ . The cross sections converge to the exact values with increasing the number of the MC configurations. The deviations become at most by  $\sim 1\%$  with  $M = 10^8$ . We note that the convergence of the cross section is much slower than that of an ordinary nuclear system, e.g.,  $^{12}\text{C}$  and  $^{20}\text{C}$  which typically need  $M = 10^6$  and  $10^7$ , respectively. More MC configurations are needed to have sufficient statistics in the tail regions of the extended wave function of  $^{22}\text{C}$ . In order to ensure the accuracy of the total reaction cross sections of  $^{22}\text{C}$  on  $^1\text{H}$  target within 1% level, we employ  $M = 10^8$  configurations for the MC integration.

Next, we apply these MC configurations to the  $^{22}\text{C} + ^{12}\text{C}$  case where the factorization method of Eq. (16) can no longer be applied. Figure 3 displays the total reaction cross sections of  $^{22}\text{C}$  on  $^{12}\text{C}$  target as a function of the rms radii. The cm contribution is exactly removed through the MC integration in Eq. (13). The trend of the cross sections with respect to  $M$  is similar to those on  $^1\text{H}$  target: The cross section distributions are scattered with  $M = 10^6$  and  $10^7$  and a monotonic and smooth increase of the cross sections is obtained with  $M = 10^8$  even at large rms radii. We confirm that one

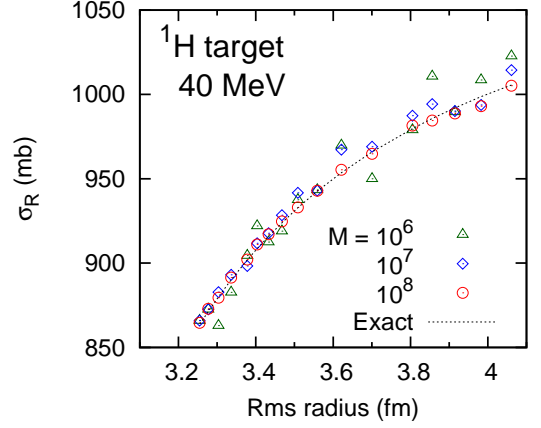


FIG. 2: Tests of total reaction cross sections of  $^{22}\text{C}$  on  $^1\text{H}$  target incident at 40 MeV as a function of the cm uncorrected rms radii with different number of the MC configurations. “Exact” values are also plotted for comparison. See text for details.

can safely use the MC configurations with  $M = 10^8$  for the multi-dimensional integration in the Glauber amplitude involving the very-extended  $^{22}\text{C}$  wave function for the analysis of the total reaction cross sections on both  $^1\text{H}$  and  $^{12}\text{C}$  targets.

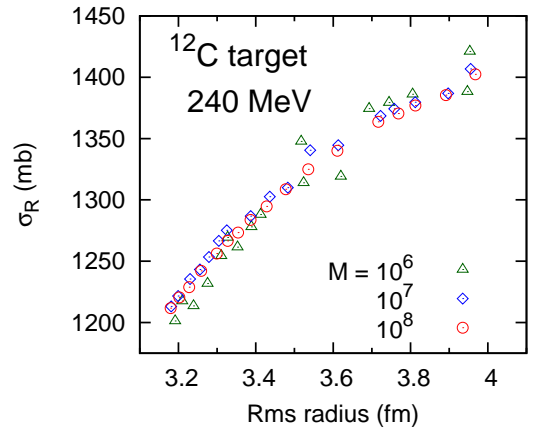


FIG. 3: Total reaction cross sections of  $^{22}\text{C}$  on  $^{12}\text{C}$  target incident at 240 MeV as a function of the center-of-mass (cm) corrected rms radii with different number of the MC configurations. The cm contribution is exactly excluded in the calculations.

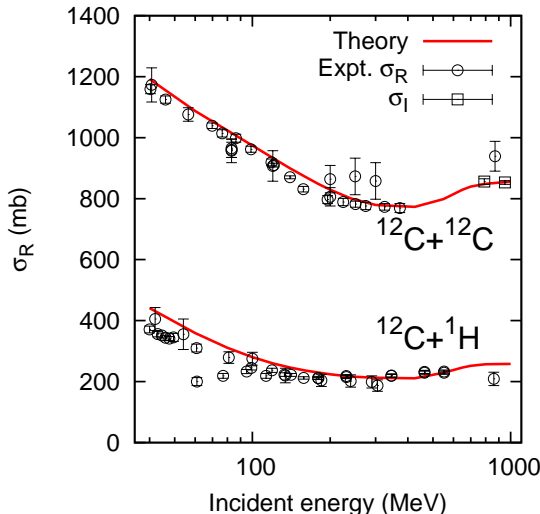


FIG. 4: Total reaction cross sections of  $^{12}\text{C}+^{12}\text{C}$  and  $^{12}\text{C}+^1\text{H}$  collisions as a function of incident energies. Experimental data of the total reaction ( $\sigma_R$ ) and interaction ( $\sigma_I$ ) cross sections are taken from Refs. [44–52] for  $^{12}\text{C}+^{12}\text{C}$  and Refs. [53, 54] for  $^{12}\text{C}+^1\text{H}$ .

#### IV. RESULTS AND DISCUSSIONS

##### A. Comparison with measured cross sections of $^{12}\text{C}$ and $^{20}\text{C}$

Thus far, we have established that the accuracy of the MC integration in the Glauber amplitude. In this subsection, we show the reliability of our approach in comparison with available experimental cross section data of  $^{12}\text{C}$  and  $^{20}\text{C}$  on  $^{12}\text{C}$  and  $^1\text{H}$  targets.

Figure 4 displays the total reaction cross sections on  $^{12}\text{C}$  and  $^1\text{H}$  targets as a function of incident energies. Our theory nicely reproduces the cross section data at the low- to high-incident energies for both  $^{12}\text{C}$  and  $^1\text{H}$  targets. The medium- to high-energy nuclear breakup processes are described systematically very well. Though the experimental data are scattered, we see, at a close look, some deviations from the experimental data with  $^1\text{H}$  target below  $\sim 100$  MeV and above  $\sim 900$  MeV from the experimental values at most by 10%.

Figure 5 plots the energy dependence of the total reaction cross sections of  $^{20}\text{C}$  on  $^{12}\text{C}$  and  $^1\text{H}$  targets. The rms radius of  $^{20}\text{C}$  is 3.03 fm which is determined so as to reproduce the interaction cross section measured at 905 MeV [42]. We confirm that our calculations are consistent with the interaction cross section data at 240 MeV on  $^{12}\text{C}$  target [12] as well as that at 40 MeV on  $^1\text{H}$  target [11].

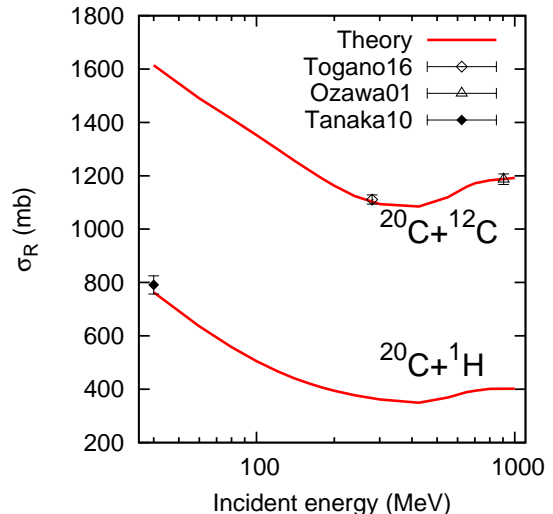


FIG. 5: Same as Fig. 4 but of  $^{20}\text{C}$ . Experimental interaction cross section data are taken from Refs. [11, 12, 42].

##### B. $^{22}\text{C}$ : Nuclear radius vs total reaction cross sections

We have shown that our theoretical model successfully describes the total reaction cross sections involving stable  $^{12}\text{C}$  and neutron-rich  $^{20}\text{C}$  at wide incident energies for both  $^{12}\text{C}$  and  $^1\text{H}$  targets in a consistent manner. Finally, let us discuss the controversy in the radius of  $^{22}\text{C}$ . Figure 6 displays the total reaction cross sections of  $^{22}\text{C}$  on  $^{12}\text{C}$  target incident at 240 MeV and on  $^1\text{H}$  target incident at 40 MeV, respectively, where the experimental data are available, as a function of the rms radius. The cross section data by Togano *et al.* [12] with uncertainties is indicated between two horizontal lines from which we can extract the rms radius of  $^{22}\text{C}$ . The resultant rms radius is  $3.38 \pm 0.10$  fm which is consistent with that extracted by Togano *et al.* using the sophisticated four-body Glauber model [55],  $3.44 \pm 0.08$  [12]. However, we find simultaneous reproduction of the cross section data by Tanaka *et al.* [11] is not possible within  $1\sigma$ , that is, for  $^1\text{H}$  target, the experimental data is far from the theoretical values (However, it is consistent with  $2\sigma$  as mentioned in Ref. [12]). Since our calculation is not feasible for very large rms radius beyond  $\sim 4$  fm, we extrapolate the rms radius with a form of  $a \log[b(R-c)]$ , where  $R = \sqrt{\langle r^2 \rangle}$ , in which  $a, b, c$  are determined by the least-square method. The extrapolated radius is huge  $\gtrsim 5$  fm at the lower limit ( $1\sigma$ ) of the experimental cross section, and never reach the central value of the experimental data 1338 mb [11] with the extrapolated function based on our theoretical cross sections.

We discuss the possible uncertainties in the theoretical calculations. We calculate the total reaction cross section on  $^1\text{H}$  target with the OLA which was employed in the analysis of Ref. [11]. The phase-shift function of the OLA

is given as the leading order of the cumulant expansion of the complete Glauber amplitude [24, 56]

$$i\chi_{\text{OLA}}(\mathbf{b}) = - \sum_{N=p,n} \int d\mathbf{r} \rho_N(\mathbf{r}) \Gamma_{pN}(\mathbf{b} - \mathbf{s}), \quad (17)$$

where  $\mathbf{r} = (\mathbf{s}, z)$  with  $\mathbf{s}$  being a two-dimensional vector perpendicular to  $z$ , and the translationally-invariant one-body density of the projectile

$$\rho_N(\mathbf{r}) = \sum_{i=1}^{N_N} \langle \Phi_N | \delta(\hat{\mathbf{r}}_i - \mathbf{r}) | \Phi_N \rangle. \quad (18)$$

where  $\hat{\mathbf{r}}_i$  denotes the  $i$ th single-particle coordinate operator measured from the cm of the system. The cm contribution in the one-body density is exactly removed through the MC integration. It is noted that this is one of the advantages of the present approach. In general, the removal of the cm contribution needs some efforts. Some approximate methods for the removal prescribed, e.g., in Refs. [41, 57] becomes worse since the square overlap of the HO and the halo wave functions of  $^{22}\text{C}$  becomes 0.82-0.85 in the present range of the rms radii, while it is larger than 0.99 for a non-halo nucleus,  $^{20}\text{C}$ .

The calculated total reaction cross sections with the OLA are displayed in Fig. 6. Here we only plot the OLA results on  $^1\text{H}$  target. More detailed comparisons between the complete Glauber calculation and the OLA approximation for nucleus-nucleus scattering are drawn in Appendix. The difference between the complete Glauber and the OLA cross sections is small approximately 1%, being the situation unchanged.

One may also think that the incident energy of 40 MeV is too low in the Glauber calculation. As shown in Figs. 4 and 5, the theory reproduces fairly well the total reaction cross section of  $^{20}\text{C}$  on  $^1\text{H}$  target even at 40 MeV. Since any excited bound state of  $^{22}\text{C}$  has not been observed so far, the total reaction and interaction cross sections are equal for  $^1\text{H}$  target and its difference is expected to be small for  $^{12}\text{C}$  target. The Coulomb breakup effect is expected to be small. For instance, the contribution is estimated less than 1% in the case of a one-neutron halo nucleus,  $^{31}\text{Ne}$  on  $^{12}\text{C}$  target [27]. It becomes even smaller in the case of  $^1\text{H}$  target. Considering the theoretical uncertainties discussed above, we conclude that the simultaneous reproduction of both the experimental cross sections on  $^{12}\text{C}$  and  $^1\text{H}$  in Refs. [11, 12] is not possible within the error bar.

Let us discuss what is actually probed by the total reaction cross sections on  $^{12}\text{C}$  and  $^1\text{H}$  targets at those specific incident energies. The total reaction cross sections at medium- to high-incident energies are closely related to the nuclear radii of colliding nuclei,  $\sigma_R \sim \pi(R_P + R_T)^2$ , where  $R_P$  ( $R_T$ ) is the nuclear radius of the projectile (target) nucleus. In fact, Figure 6 shows good proportionality of the cross sections on the rms radii and this enhancement is similar for  $^{12}\text{C}$  and  $^1\text{H}$  targets. It is interesting to note that this increase becomes moderate for

large rms radii. To confirm whether this effect is due to the halo structure or not, we generate a “standard” nucleus by assuming for the  $^{22}\text{C}$  wave function the product of the HO single-particle wave functions. The cross sections with the HO wave function are plotted in Fig. 6 as a function of the rms radii which are controlled by the HO oscillator length parameter. The cross section firmly increases as the rms radius increases which is in contrast to the case with the halo wave function.

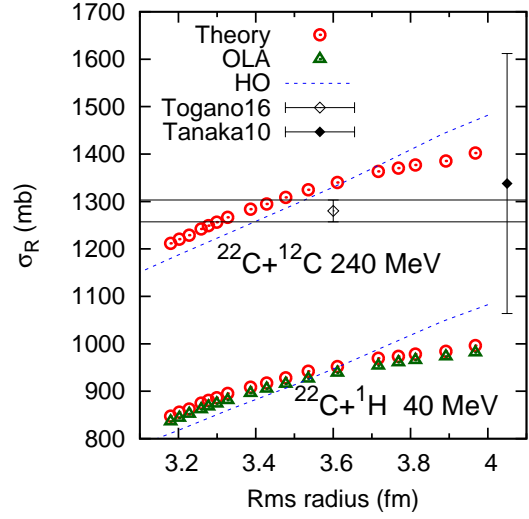


FIG. 6: Total reaction cross sections of  $^{22}\text{C}$  on  $^{12}\text{C}$  and  $^1\text{H}$  incident at 240 MeV and 40 MeV, respectively, as a function of rms radii of  $^{22}\text{C}$ . Thin lines denote the cross sections with the harmonic-oscillator (HO) wave function. See text for details. Experimental data are taken from Refs. [11, 12].

In order to clarify the reasons of the different cross section enhancement with the halo and HO wave functions, we show the evolution of the reaction probabilities defined in Eq. (3) with respect to the rms radius  $R$ . For this purpose, we calculate the difference between two reaction probabilities defined by

$$D_R(\mathbf{b}) = P(\mathbf{b})|_R - P(\mathbf{b})|_{R=3.20}, \quad (19)$$

where the probability with the  $^{22}\text{C}$  wave function which gives  $R = 3.20$  fm is subtracted to see clearly changes of the probabilities, Figure 7 plots  $D_R$  calculated with the halo and HO wave functions as a function of the impact parameter  $b = |\mathbf{b}|$ . For both  $^{12}\text{C}$  and  $^1\text{H}$  targets, the behavior of  $D_R$  with the halo and HO wave functions are quite different: The enhancement of the reaction probability becomes smaller and smaller with increasing the rms radius in the case of the halo wave function, whereas  $D_R$  increases monotonically in the case of the HO wave function. For the halo wave function, since this is very much extended, only the weakly-bound two-neutron wave function is contributed to the enhancement of  $D_R$ . With large  $R$ , only dilute neutron tail contributes to the nuclear radius but not much to the total reaction cross sec-

tion, leading to the moderate increase of the cross sections with large  $R$  observed in Fig. 6. In the case of the HO wave function, all nuclear orbits extend with increasing the HO oscillator length that results in the monotonic increase of the cross sections.

We note, however, the difference of the reaction probabilities displayed in Fig. 7 appears to be similar in both  $^{12}\text{C}$  and  $^1\text{H}$  targets. This indicates that the sensitivity of the density profile of the projectile does not depend much on the target nuclei,  $^{12}\text{C}$  and  $^1\text{H}$ , for this set of the incident energies. Since the  $pn$  total cross section as well as the range of the interaction become large in such a low incident energy, the contribution involving the two-neutron halo tail becomes significant being comparable to the case of  $^{12}\text{C}$  target. The fact is consistent with the discussion given in Ref. [26] that showed the advantage of using the low energy nuclear reaction with  $^1\text{H}$  target to probe the neutron distribution, where the  $pn$  total cross section becomes much larger than that of the  $pp$  one. This can also be seen in comparison of the ordinary nucleus,  $^{12}\text{C}$ , and neutron-rich  $^{20}\text{C}$  reactions on  $^1\text{H}$  target displayed in Figs. 4 and 5.

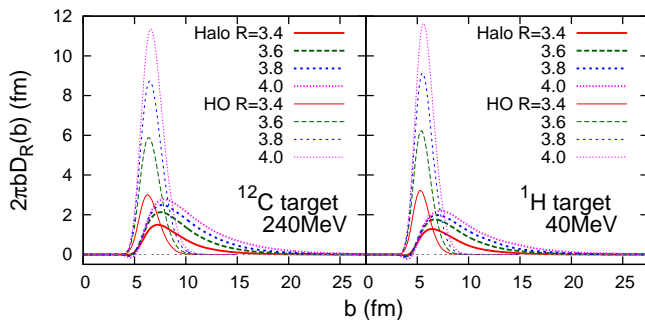


FIG. 7: Difference between two reaction probabilities of the  $^{22}\text{C}$  wave functions with different rms radii on  $^{12}\text{C}$  target at 240 MeV and on  $^1\text{H}$  target at 40 MeV as a function of impact parameters. The reference reaction probability ( $R = 3.20$ ) is subtracted from each probabilities with  $R = 3.40, 3.60, 3.80$ , and  $4.00$  fm. See text for details. Thick lines denote the results with the halo wave functions, while thin lines denote those with the HO wave functions.

Finally, we plot, in Fig. 8, the theoretical total reaction cross sections of  $^{22}\text{C}$  as a function of the incident energies together with the available interaction cross section data [11, 12]. We employ the wave function giving  $R = 3.38 \pm 0.10$  fm taken consistently with the recent interaction cross section data [12]. We again confirm that the target dependence is not large at 40 MeV for  $^1\text{H}$  target and at 240 MeV for  $^{12}\text{C}$  target, that is, the cross section variation with respect to the radius change is almost the same. The cross sections on  $^{12}\text{C}$  target have some sensitivity of the halo tail at any incident energies, whereas the ones on  $^1\text{H}$  target lose the sensitivity with increasing the incident energy as the  $pn$  total cross section becomes smaller. In the figure, one can clearly see that the simultaneous reproduction of the two experimental

data within the error bar is not feasible. Since we have only two experimental cross section data, it is desired to have another data at different incident energy or target in order to clarify that the  $^{22}\text{C}$  size is equivalent to a radius of medium- ( $A \sim 40$ ) or heavy- ( $A \sim 200$ ) mass nuclei. However, we already see theoretical consistency with the  $^{20}\text{C}$  cross section data for both  $^1\text{H}$  and  $^{12}\text{C}$  target in Fig. 5. It is unlikely to have a huge radius  $\gtrsim 5$  fm of  $^{22}\text{C}$ .

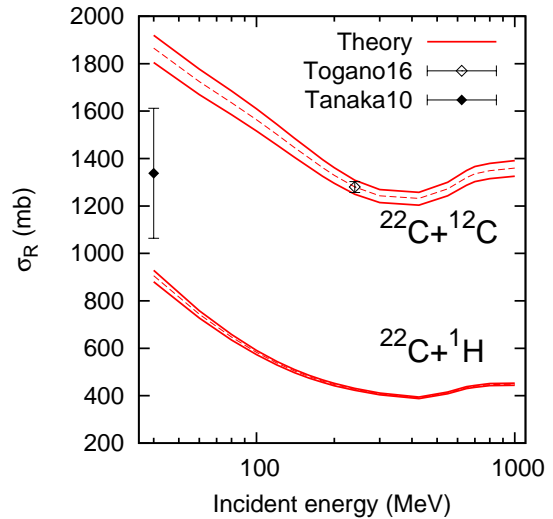


FIG. 8: Total reaction cross sections of  $^{22}\text{C}$  on  $^{12}\text{C}$  and  $^1\text{H}$  targets as a function of incident energies. The rms radius of  $^{22}\text{C}$  is set to be  $3.38 \pm 0.10$  fm. The central value and the lower and upper bounds of the cross sections are indicated by dotted and solid lines, respectively. Experimental data are taken from Refs. [11, 12].

## V. CONCLUSION

In order to resolve the radius puzzle in  $^{22}\text{C}$ , we have investigated the total reaction cross sections of  $^{22}\text{C}$  on  $^{12}\text{C}$  and  $^1\text{H}$  targets incident at medium- to high-incident energies within the framework of a microscopic high-energy reaction theory, the Glauber model. The complete optical phase-shift function or Glauber amplitude in the Glauber model is evaluated with use of a Monte Carlo technique.

The calculated total reaction cross sections on  $^{12}\text{C}$  and  $^1\text{H}$  targets consistently reproduce the available experimental cross section data for  $^{12}\text{C}$  and  $^{20}\text{C}$ . We find that target dependence of the radius extraction of  $^{22}\text{C}$  is small at 240 MeV for  $^{12}\text{C}$  target and 40 MeV for  $^1\text{H}$  target. We see, however, the simultaneous reproduction of the interaction cross section data of  $^{22}\text{C}$  obtained by the two recent measurement is not possible within the error bar ( $1\sigma$ ). The root-mean-square (rms) matter radius of  $^{22}\text{C}$  deduced from our analysis is consistent with the radius



given in Ref. [12] using the interaction cross section incident on  $^{12}\text{C}$  target at 240 MeV, which corresponds to that of an  $A \sim 40$  nucleus. We investigate possible uncertainties in the theoretical model and they are actually small. We conclude that it is unlikely to obtain the huge rms matter radius of  $\sim 5.4$  fm ( $A \sim 200$ ) shown in Ref. [11].

### Acknowledgments

The authors thank J. Singh for careful reading of the manuscript. This work was in part supported by JSPS KAKENHI Grant Numbers 18K03635 and 18H04569.

### Appendix A: Comparison with other approximations of the Glauber theory

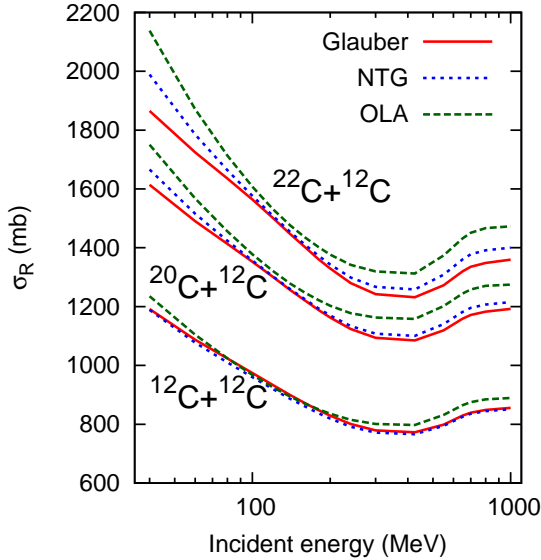


FIG. 9: Total reaction cross sections of  $^{12}\text{C}$ ,  $^{20}\text{C}$ , and  $^{22}\text{C}$  on  $^{12}\text{C}$  target as a function of incident energies calculated with the complete Glauber amplitude, the NTG approximation, and the OLA. See text for details. The rms radii of  $^{12}\text{C}$ ,  $^{20}\text{C}$ , and  $^{22}\text{C}$  employed in the calculations are 2.33, 3.03, and 3.38 fm, respectively.

In this appendix, we evaluate standard approximate methods of the Glauber theory and quantify theoretical uncertainties in nucleus-nucleus total reaction cross section calculations. In general, the evaluation of the complete Glauber amplitude of Eq. (2) requires tedious computations. Therefore, the so-called optical-limit approximation (OLA) has often been used as it only requires one-body density distributions of the projectile and target nuclei. This approximation relies on the cumulant expansion [24, 56] which offers series expansion in terms of the fluctuation of the distribution function. The expansion works well for such nuclei having a standard

density profile. Contribution of the higher-order terms becomes more important for an extended density distribution such as halo nuclei. In fact, the standard OLA, which only takes the leading term of the expansion, cannot be applied to nucleus-nucleus reactions involving halo nuclei as it leads to some systematic uncertainties on the extraction of the nuclear radii [34, 35].

Though the OLA only takes the leading order of the consecutive product of the  $NN$  phase-shift functions, the approximation already works well for the total reaction cross sections on  $^1\text{H}$  target even they involve a halo nucleus as shown in Refs. [30, 36] as well as in Fig. 6 of the present paper. The phase-shift function of the OLA is given as the leading order of the cumulant expansion of the complete Glauber amplitude [24, 56]

$$i\chi_{\text{OLA}}(\mathbf{b}) = - \sum_{N,N'=n,p} \iint d\mathbf{r} d\mathbf{r}' \times \rho_N^P(\mathbf{r}) \rho_{N'}^T(\mathbf{r}') \Gamma_{NN'}(\mathbf{b} + \mathbf{s} - \mathbf{s}'), \quad (\text{A1})$$

where  $\rho_N^P$  ( $\rho_N^T$ ) is the translationally-invariant one-body density of the projectile (target) for proton  $N = p$  and neutron  $N = n$  defined in Eq. (18).

For nucleus-nucleus scattering, where the higher-order contribution would be sizable, the Nucleon-Target formalism in the Glauber theory (NTG) [58], has often been used:

$$i\chi_{\text{NTG}}(\mathbf{b}) = -\frac{1}{2} \sum_{N,N'=n,p} \left\{ \int d\mathbf{r} \rho_N^P(\mathbf{r}) \times \left[ 1 + \exp \left( - \int d\mathbf{r}' \rho_{N'}^T(\mathbf{r}') \Gamma_{NN'}(\mathbf{b} + \mathbf{s} - \mathbf{s}') \right) \right] + \int d\mathbf{r}' \rho_{N'}^T(\mathbf{r}') \times \left[ 1 + \exp \left( - \int d\mathbf{r} \rho_N^P(\mathbf{r}) \Gamma_{NN'}(\mathbf{b} + \mathbf{s}' - \mathbf{s}) \right) \right] \right\}. \quad (\text{A2})$$

Note that the same inputs of the OLA are required. The NTG approximation has been applied to a number of examples in the nucleus-nucleus total reaction cross section calculations including stable and neutron-rich isotopes [2, 18, 23, 27–29, 41, 59–63]. Here we quantify the extent to which the higher-order terms are included in the NTG approximation in comparison with the complete Glauber calculation and the standard OLA.

Figure 9 plots the total reaction cross sections of  $^{12}\text{C}$ ,  $^{20}\text{C}$ , and  $^{22}\text{C}$  on  $^{12}\text{C}$  target as a function of the incident energies calculated with the complete Glauber amplitude (2), the NTG approximation (A2), and the OLA (A1). The wave functions of those nuclei are taken consistently with the charge radius for  $^{12}\text{C}$ , and the interaction cross sections at 900 MeV [42] for  $^{20}\text{C}$  and at 240 MeV [12] for  $^{22}\text{C}$ . For  $^{12}\text{C}+^{12}\text{C}$  scattering, as already exemplified in Refs. [18, 41], we again confirm that the NTG gives better results than those obtained by the OLA and takes care of most of the multiple-scattering effects

missing in the OLA, showing the cross sections much closer to the complete Glauber calculations. The NTG approximation also works well for  $^{20}\text{C}$  but large deviation appears with the OLA. For  $^{22}\text{C}$ , as expected, the OLA considerably deviates from the calculated cross sections obtained with the complete Glauber amplitude. The deviations of these approximations from the complete calculation appear to be minimum at around 100-200 MeV. The NTG always gives better results than those of the OLA but it is still not sufficient at low- and high-incident energies, say 3% deviation at 1000 MeV from the complete calculation. Though the deviations of these approximations are smaller at 240 MeV, these theoretical

uncertainties actually affect the radius extraction from the measured cross section data [12]: The extracted radii are  $R = 3.33 \pm 0.09$  and  $3.23 \pm 0.07$  fm with the NTG and OLA, respectively, while  $R = 3.38 \pm 0.10$  fm with the complete Glauber calculation. The deviations become even larger with increasing the halo tail and at different incident energies. Here we have seen that the NTG approximation works well for the standard density profile but not for the halo density. One needs to care about the uncertainties included in these approximations when the nuclear radius is extracted from the total reaction cross section on  $^{12}\text{C}$  target.

- 
- [1] I. Tanihata, H. Hamagaki, O. Hashimoto, Y. Shida, N. Yoshikawa *et al.*, Phys. Rev. Lett. **55**, 2676 (1985).
  - [2] W. Horiuchi and Y. Suzuki, Phys. Rev. C **74** 034311 (2006).
  - [3] G. Audi, A. H. Wapstra, and C. Thibault, Nucl. Phys. **A 729**, 337 (2003).
  - [4] L. Gaudefroy, W. Mittig, N. A. Orr, S. Varet, M. Chartier *et al.*, Phys. Rev. Lett. **109**, 202503 (2012).
  - [5] N. Kobayashi, T. Nakamura, J. A. Tostevin, Y. Kondo, N. Aoi *et al.*, Phys. Rev. C **86**, 054604 (2012).
  - [6] M. T. Yamashita, R. S. Marques de Carvalho, T. Frederico, and L. Tomio, Phys. Lett. **B 697**, 90 (2011).
  - [7] B. Acharya, C. Ji, and D. R. Phillips, Phys. Lett. **B 723**, 196 (2013).
  - [8] S. N. Ershov, J. S. Vaagen, and M. V. Zhukov, Phys. Rev. C **86**, 034331 (2012).
  - [9] K. Ogata, T. Myo, T. Furumoto, T. Matsumoto, and M. Yahiro, Phys. Rev. C **88**, 024616 (2013).
  - [10] T. Inakura, W. Horiuchi, Y. Suzuki, and T. Nakatsukasa, Phys. Rev. C **89**, 064316 (2014).
  - [11] K. Tanaka, T. Yamaguchi, T. Suzuki, T. Ohtsubo, M. Fukuda *et al.*, Phys. Rev. Lett. **104**, 062701 (2010).
  - [12] Y. Togano, T. Nakamura, Y. Kondo, J. A. Tostevin, A. T. Saito *et al.*, Phys. Lett. **B 761**, 412-418 (2016).
  - [13] H. T. Fortune and R. Sherr, Phys. Rev. C **85**, 027303 (2012).
  - [14] M. Takechi, T. Ohtsubo, T. Kuboki, M. Fukuda, D. Nishimura *et al.*, Mod. Phys. Lett. **A 25**, 1878 (2010).
  - [15] K. Minomo, T. Sumi, M. Kimura, K. Ogata, Y. R. Shimizu, and M. Yahiro, Phys. Rev. C **84**, 034602 (2011).
  - [16] K. Minomo, T. Sumi, M. Kimura, K. Ogata, Y. R. Shimizu, and M. Yahiro, Phys. Rev. Lett. **108**, 052503 (2012).
  - [17] T. Sumi, K. Minomo, S. Tagami, M. Kimura, T. Matsumoto *et al.*, Phys. Rev. C **85**, 064613 (2012).
  - [18] W. Horiuchi, T. Inakura, T. Nakatsukasa, and Y. Suzuki, Phys. Rev. C **86**, 024614 (2012).
  - [19] S. Watanabe, K. Minomo, M. Shimada, S. Tagami, M. Kimura *et al.*, Phys. Rev. C **89**, 044610 (2014).
  - [20] M. Takechi, S. Suzuki, D. Nishimura, M. Fukuda, T. Ohtsubo *et al.*, Phys. Rev. C **90**, 061305(R) (2014).
  - [21] W. Horiuchi, T. Inakura, T. Nakatsukasa, and Y. Suzuki, JPS Conf. Proc. **6**, 030079 (2015).
  - [22] W. Horiuchi, Y. Suzuki, and T. Inakura, Phys. Rev. C **89**, 011601 (R) (2014).
  - [23] W. Horiuchi, S. Hatakeyama, S. Ebata, and Y. Suzuki, Phys. Rev. C **93**, 044611 (2016).
  - [24] R. J. Glauber, *Lectures in Theoretical Physics*, edited by W. E. Brittin and L. G. Dunham (Interscience, New York, 1959), Vol. 1, p.315.
  - [25] L. Ray, Phys. Rev. C **20**, 1857 (1979).
  - [26] B. Abu-Ibrahim, W. Horiuchi, A. Kohama, and Y. Suzuki, Phys. Rev. C **77**, 034607 (2008); *ibid* **80**, 029903 (2009); **81**, 019901 (2010).
  - [27] W. Horiuchi, Y. Suzuki, P. Capel, and D. Baye, Phys. Rev. C **81**, 024606 (2010).
  - [28] B. Abu-Ibrahim, S. Iwasaki, W. Horiuchi, A. Kohama, and Y. Suzuki, J. Phys. Soc. Jpn., Vol. 78, 044201 (2009).
  - [29] W. Horiuchi, S. Hatakeyama, S. Ebata, and Y. Suzuki, Phys. Rev. C **96**, 024605 (2017).
  - [30] B. Abu-Ibrahim, K. Fujimura, and Y. Suzuki, Nucl. Phys. **A 657**, 391 (1999).
  - [31] R. H. Bassel and C. Wilkin, Phys. Rev. **174**, 1179 (1968).
  - [32] S. Hatakeyama, S. Ebata, W. Horiuchi, and M. Kimura, J. Phys.: Conf. Ser. **569**, 012050 (2014).
  - [33] S. Hatakeyama, S. Ebata, W. Horiuchi, and M. Kimura, JPS Conf. Proc., Vol. **6**, 030096 (2015).
  - [34] J. S. Al-Khalili and J. A. Tostevin, Phys. Rev. Lett. **76**, 3903 (1996).
  - [35] J. S. Al-Khalili, J. A. Tostevin, and I. J. Thompson, Phys. Rev. C **54**, 1843 (1996).
  - [36] K. Varga, S. C. Pieper, Y. Suzuki, and R. B. Wiringa, Phys. Rev. C **66**, 034611 (2002).
  - [37] B. Abu-Ibrahim, Y. Ogawa, Y. Suzuki, and I. Tanihata, Comp. Phys. Commun. **151**, 369 (2003).
  - [38] W. R. Gibbs and J. P. Dedonder, Phys. Rev. C **86**, 024604 (2012).
  - [39] I. Angeli, K. P. Marinova, At. Data. Nucl. Data Tables **99**, 69 (2013).
  - [40] A. Bohr and B. R. Mottelson, Nuclear Structure, Vol. I & II (W. A. Benjamin, New York, 1975).
  - [41] W. Horiuchi, Y. Suzuki, B. Abu-Ibrahim, and A. Kohama, Phys. Rev. C **75**, 044607 (2007).
  - [42] A. Ozawa, O. Bochkarev, L. Chulkov, D. Cortina, H. Geissel *et al.*, Nucl. Phys. **A 691**, 599 (2001).
  - [43] N. Metropolis, A. Rosenbluth, M. Rosenbluth, E. Teller, J. Chem. Phys. **21**, 1087 (1953).
  - [44] M. Takechi, M. Fukuda, M. Mihara, T. Chinda, T. Matsumasa *et al.*, Eur. Phys. J. A **25**, s01, 217 (2005) and private communication.

- [45] C. Perrin, S. Kox, N. Longequeue, J. B. Viano, M. Buenerd *et al.*, Phys. Rev. Lett. **49**, 1905 (1982).
- [46] H.Y. Zhang, W.Q. Shen, Z.Z. Ren, Y.G. Ma, W. Z. Jiang *et al.*, Nucl. Phys. **A 707**, 303 (2002).
- [47] D.Q. Fang, W.Q. Shen, J. Feng, X. Z. Cai, J. S. Wang *et al.*, Phys. Rev. C **61**, 064311 (2000).
- [48] S. Kox, A. Gamp, C. Perrin, J. Arvieux, R. Bertholet *et al.*, Phys. Rev. C **35**, 1678 (1987).
- [49] T. Zheng, T. Yamaguchi, A. Ozawa, M. Chiba, R. Kanungo *et al.*, Nucl. Phys. **A 709**, 103 (2002).
- [50] J. Y. Hostachy, M. Buenerd, J. Chauvin, D. Lebrun, Ph. Martin *et al.*, Nucl. Phys. **A 490**, 441 (1988).
- [51] J. Jaros, A. Wagner, L. Anderson, O. Chamberlain, R. Z. Fuzesy *et al.*, Phys. Rev. C **18**, 2273 (1978).
- [52] A. Ozawa, T. Suzuki, I. Tanihata, Nucl. Phys. **A 693**, 32 (2001).
- [53] R. F. Carlson, At. Dat. Nucl. Dat. Tables **63**, 93 (1996).
- [54] A. Auce, A. Ingemarsson, R. Johansson, M. Lantz, G. Tibell *et al.*, Phys. Rev. C **71**, 064606 (2005).
- [55] Y. Kucuk and J. A. Tostevin, Phys. Rev. C **89**, 034607 (2014).
- [56] Y. Suzuki, R. G. Lovas, K. Yabana, and K. Varga, *Structure and reactions of light exotic nuclei* (Taylor & Francis, London, 2003).
- [57] J. W. Negele, Phys. Rev. C **1**, 1260 (1970).
- [58] B. Abu-Ibrahim and Y. Suzuki, Phys. Rev. C **61**, 051601(R) (2000).
- [59] M. Takechi, M. Fukuda, M. Mihara, K. Tanaka, T. Chinda *et al.*, Phys. Rev. C **79**, 061601(R) (2009).
- [60] K. Hagino and H. Sagawa, Phys. Rev. C **84**, 011303(R) (2011).
- [61] R. Kanungo, A. Prochazka, W. Horiuchi, C. Nociforo, T. Aumann *et al.*, Phys. Rev. C **83**, 021302(R) (2011).
- [62] R. Kanungo, A. Prochazka, M. Uchida, W. Horiuchi, G. Hagen *et al.*, Phys. Rev. C **84**, 061304(R) (2011).
- [63] Y. Urata, K. Hagino, and H. Sagawa, Phys. Rev. C **96**, 064311 (2017).